THE JOURNAL OF PHYSICAL CHEMISTRY LETTERS
A JOURNAL OF THE AMERICAN CHEMICAL SOCIETY

pubs.acs.org/JPCL

Letter

Enhanced Urea Oxidation Electrocatalytic Activity by Synergistic Cobalt and Nickel Mixed Oxides

Tongxin Zhou, Sathya Narayanan Jagadeesan, Lihua Zhang, N. Aaron Deskins, and Xiaowei Teng*

Cite This: *J. Phys. Chem. Lett.* 2024, 15, 81−89

Read Online

ACCESS | Metrics & More | Article Recommendations | Supporting Information

ABSTRACT: Exploring reactive and selective Ni-based electrocatalysts for the urea oxidation reaction (UOR) is crucial for developing urea-related energy conversion technologies. Herein, synergistic interactions in Ni/Co mixed oxides/hydroxides enhanced the UOR with low onset potential, fast reaction kinetics, and good selectivity against the oxygen evolution reaction (OER). Our electrochemical measurements and theoretical calculations signified the collaborative interaction of Ni/Co mixed oxide/hydroxide heterostructures to enhance UOR activity. Our results showed that Ni^{3+} species, formed at high anodic potential, produced a high anodic current primarily from unwanted OER. Instead, the Ni/Co heterostructures with dominant Ni^{2+} and Co^{3+} species remained stable at low anodic potential and exhibited anodic current exclusively attributed to UOR. This work highlights the importance of tuning valence charges for designing high-performance and selective UOR electrocatalysts to benefit the environmental remediation of urea runoff and enable urea electrolysis for hydrogen production by replacing conventional OER with UOR at the anode.

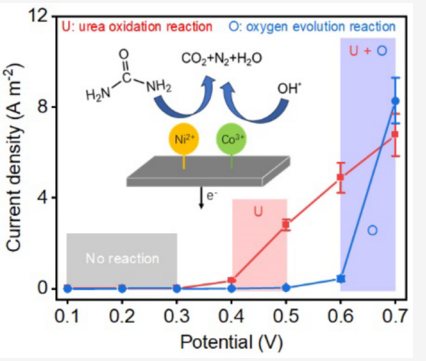

Hydrogen is increasingly crucial for carbon-neutral energy systems. However, economically viable hydrogen production via water electrolysis is limited mainly by the sluggish kinetics of the oxygen evolution reaction (OER, eq 1).[1] Although significant efforts have been made to design OER catalysts with reduced overpotential and improved stability, there is emerging research interest in the electrolysis of small organic molecules (SOMs) for hydrogen production. There is interest in the electrooxidation of methanol, ethanol, or urea fuels as an alternative to the OER at the anode due to the lower overpotential required to drive SOMs oxidation compared to OER.[2] Compared to alcohols, urea has several unique characteristics, making it a potential hydrogen storage medium that could offer viable on-demand hydrogen production. For instance, urea is nontoxic, has high water solubility, and has high hydrogen content (6.7 wt %).[2] In addition, the equilibrium potential ($E^{\ominus}_{A)}$) for the urea oxidation reaction (UOR, eq 2) is −0.46 V (vs SHE at pH 14) at the anode. Given that the hydrogen evolution reaction (HER) happens at a theoretical potential ($E^{\ominus}_{C}$) of −0.83 V at the cathode, the urea electrolysis alkaline cell at pH 14 offers a theoretical cell voltage window of 0.37 V ($E^{\ominus}_{A} - E^{\ominus}_{C}$), much narrower than water electrolysis (1.23 V). Thus, urea electrolysis for hydrogen production is more energy-efficient and economical than water electrolysis.[3−5]

As the major nitrogen fertilizer and feed additive, urea was commercially produced as early as the 1920s with the Haber−Bosch process and was produced globally with ∼180 million metric tons in 2021.[6] Besides catalytical production, urea can be derived from natural sources, where an adult produces 1.5 L of urine daily, equivalent to 11 kg of urea and 0.77 kg of hydrogen gas yearly. While urea is a low-cost nitrogen agriculture fertilizer and a natural product from human metabolism, urea-rich agricultural runoff and municipal wastewater discharge cause eutrophication with harmful algal blooms and hypoxic dead zones, adversely impacting the aquatic environment and human health.[7] Therefore, utilizing urea in waste streams through electrolysis processes facilitates energy-efficient production of hydrogen fuel and sequesters urea from water to maintain the long term sustainability of ecological systems, bringing a revolutionary impact on the water-energy nexus.[8]

$$4OH^- \rightarrow O_2 + 2H_2O + 4e^- \quad (1)$$

$$CO(NH_2)_2 + 6OH^- \rightarrow 6e^- + N_2 + CO_2 + 5H_2O \quad (2)$$

$$Ni(OH)_2 + OH^- \rightarrow NiOOH + e^- + H_2O \quad (3)$$

$$CO(NH_2)_2 + H_2O + 6NiOOH \rightarrow 6Ni(OH)_2 + N_2 + CO_2 \quad (4)$$

Although urea electrolysis is of great importance in environmental remediation and energy technologies, the UOR suffers

Received: November 20, 2023
Revised: December 19, 2023
Accepted: December 20, 2023
Published: December 22, 2023

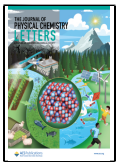

https://doi.org/10.1021/acs.jpclett.3c03257
J. Phys. Chem. Lett. 2024, 15, 81−89

from intrinsically sluggish kinetics due to a complex six-electron transfer process and the interference of water electrolysis.[9] Great advances have been made in nickel-based catalysts to catalyze the UOR as alternatives to precious metals, including oxides/hydroxides,[10] cyanides,[11] nitrides,[12] and alloys.[13] However, the UOR-active phases of Ni-based electrocatalysts still need to be experimentally elucidated. Several studies suggested that high-valence Ni^{3+} species are active toward UOR in alkaline media. They proposed two generalized mechanisms, including direct and indirect pathways, to describe possible steps through which the UOR may take place on high-valence Ni-based hydroxides/oxyhydroxides.[14,15] It was suggested that Ni^{2+} species, in the form of NiO or $Ni(OH)_2$, were oxidized electrochemically to the catalytically active 3+ oxidation state (e.g., NiOOH, eq 3). The electrooxidation of urea could be catalyzed by NiOOH (eq 2) in a direct pathway. Alternatively, urea reacted with Ni^{3+} species to form CO_2, N_2, and H_2O products while regenerating the Ni^{2+} catalyst via a nonelectrochemical step (eq 4) via an indirect pathway.

Notably, the mechanisms described above based on the NiOOH active phase for UOR have been challenged by several recent studies, suggesting that Ni species, other than Ni^{3+}, were more active toward UOR in alkaline media. For example, a lattice-oxygen-involved UOR reaction mechanism was studied, suggesting Ni^{4+} might be a more UOR-active phase.[16] On the contrary, recent work on $Ni_2Fe(CN)_6$ electrocatalysts showed that both Fe^{2+} and Ni^{2+} species were not oxidized to FeOOH and NiOOH even after a long-term UOR process, suggesting low-valence transition metals (e.g., Fe^{2+} and Ni^{2+}) can be active species for a highly stable UOR electrocatalyst.[11] Therefore, explicit evidence of the Ni active phase/valence and reaction mechanism is still unsettled, which requires detailed electrochemical measurements coupled with *in situ* spectroscopic analysis.

While Ni species have been considered the most promising UOR electrocatalysts in alkaline media, experimental and computational studies also pointed out the necessity of forming multicomponent electrocatalysts to mitigate surface blockage of reaction intermediates and increase UOR kinetics.[17] Such synergistic effects have been demonstrated in multicomponent Ru−Ni,[18] Ni−Fe−O,[4,19] Ni−Mo−O,[20] and Ni−Co−Ge-O[21] catalysts, where one component promotes the deprotonation reactions, and the other component facilitates the generation of reactive hydroxyl radicals (*OH) on the catalyst surface as an oxidant agent to react with urea molecules and reaction intermediates (e.g., *CO $(NH)_2$, *CO $(N)_2$, or *CO) for the complete oxidation to CO_2, N_2, and H_2O. Notably, the generation of *OH from the dissociative adsorption of water on the catalyst surface requires high anodic potential, which, on the other hand, could cause structure reconstruction or even impair the catalyst stability. In addition, the high anodic potential could also trigger the OER, as water dissociation is one of the first elementary steps of the OER and thus impairs the Coulombic efficiency of electrochemical processes. Therefore, it remains a tough challenge and technically significant to design Ni-based oxides that are highly stable, retain the catalytically active crystalline phase, and can also form reactive oxygen species (e.g., *OH) via water activation to selectively react and remove surface blocked *CO species to promote complete UOR versus the O_2 formation via OER.

In this study, enhanced electrocatalytic UOR activity was observed in homogeneously mixed Ni/Co oxide and hydroxide heterostructures. Synergistic effects indicated a decreasing onset potential (0.39 V vs Hg/HgO at a current density of 1 A/m^2) and improved UOR reaction kinetics (a Tafel slope of 77.7 mV dec^{-1}), superior to NiO (0.45 V and 112.8 mV dec^{-1}), NiOOH (0.54 V and 200.5 mV dec^{-1}), Co_3O_4 (0.65 V and 101.5 mV dec^{-1}), and commercial Pd/C catalysts (0.49 V and 193.8 mV dec^{-1}). Our results not only support the electrooxidation mechanism in UOR (direct pathway, eq 2) but also elucidate the complex role of Ni and Co valence in catalyzing UOR against unwanted OER via staircase voltammetry electrochemical measurements, synchrotron X-ray absorption spectroscopy, X-ray diffraction, and XPS analysis. We discovered that Ni/Co oxide heterostructures have dominant Ni^{2+} and Co^{3+} species that could catalyze the UOR with nearly 100% Coulombic efficiency without triggering the OER. Unlike previous studies suggesting high-valence-Ni (Ni^{3+} or Ni^{4+}) is highly active for UOR, our results showed that Ni^{3+} species, formed at high anodic potential, indeed produced a high anodic current; however, a large portion of the anodic current was from unwanted OER. Instead, the Ni/Co mixed oxide heterostructures Ni^{2+} and Co^{3+} remain stable at a relatively low anodic potential and exhibit anodic current exclusively attributed to UOR. The density functional theory (DFT) calculations show that mixed Ni/Co oxides have altered electronic states, thereby promoting the UOR.

Figure S1a shows the crystallographic structures of the Ni/Co oxide samples prepared by the hydrothermal method and examined by synchrotron XRD and Rietveld refinement. All the diffraction peaks can be indexed to Ni or Co oxides ($M^{II}O$), spinel ($M^{II,III}{}_3O_4$), and hydroxides ($M^{II}(OH)_2$) with corresponding weight ratios of 53.1%, 38.0%, and 8.9%, respectively. Although oxyhydroxide ($M^{III}OOH$) did not exist in the pristine Ni/Co catalysts, it appeared (with a weight ratio of ∼11.5%) after UOR (Figure S1b). Notably, XRD may not be sufficient to differentiate between Co and Ni oxides/hydroxides. Cobalt and nickel are neighboring elements in the periodic table with similar electronic structures and interactions with X-rays. In addition, Co and Ni oxides/hydroxides have similar crystal structures (e.g., atomic radii, interatomic distances, and bond lengths). Therefore, these similarities lead to comparable XRD patterns of Co and Ni oxides/hydroxides, making it difficult to differentiate the element-specific phases using XRD alone. Scanning transmission electron microscopy (STEM) equipped with EDS elementary mapping was used to examine the morphology and microstructure of the sample for a more comprehensive understanding of the Ni and Co distribution within the sample. Figure 1a shows the high-angle annular dark field (HAADF) of the Ni/Co, showing hexagon-shaped planar particles, agreeing with morphologies reported in Ni- and Co-based mixed oxides/hydroxides.[5] The elemental mapping signals from Ni, Co, and combined Ni and Co are presented in Figures 1b−d to visualize the compositional homogeneities in the Ni/Co sample. While the crystalline phases remain of great complexity, including MO, $M(OH)_2$, and M_3O_4, the STEM-EDS elemental mapping indicates a uniform distribution of Ni and Co within a large area of particles. The Ni and Co molar ratio from STEM-EDS mapping is calculated to be 51.1% and 48.9%, in line with the precursor ratio during the synthesis.

https://doi.org/10.1021/acs.jpclett.3c03257
J. Phys. Chem. Lett. 2024, 15, 81−89

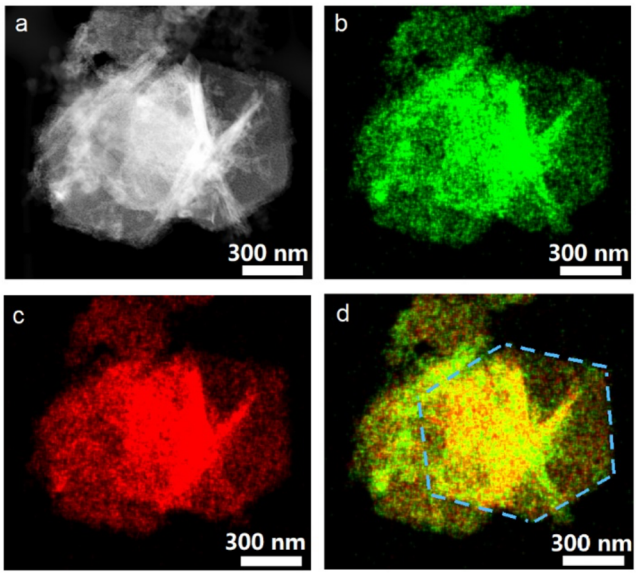

Figure 1. (a) HAADF image and elemental mapping of (b) Co (green), (c) Ni (red), and (d) combined Ni and Co.

The electrocatalytic performance of the Ni/Co heterostructure (mixed with 30 wt % active carbon) toward the UOR was tested in a standard three-electrode configuration using various NaOH (0.1−3 M) and urea concentrations (0.001−3 M), as shown in Figure S2. A solution containing 2 M NaOH and 1 M urea was finally chosen for its optimum UOR performance. The electrochemically active surface areas (ECSAs) of electrocatalysts are estimated by measuring the double-layer capacitance of the catalytic surface.[22] ECSAs of the electrocatalysts involved in this study are shown in Figure S3 and Table S1. All of the current density data presented in this study are ECSA-specific values. Figure 2 shows the linear sweep voltammetry (LSV) curves of Ni/Co, along with benchmark commercial carbon-supported Pd catalysts (Pd/C, Premetek, 20% metal loading by mass), studied in 2 M NaOH and 2 M NaOH/1 M urea electrolytes, respectively (complete cyclic voltammetry data are shown in Figure S4). Clearly, Ni/Co decreased the energy barrier to catalyze UOR, requiring a potential of 0.39 V much lower than that of Pd/C (0.49 V) to deliver a current density of 1 A m^{-2}. Figure 2b shows that the OER occurs when the potential increases beyond ∼0.6 V in 2 M NaOH solution, and the current increases rapidly with the increasing potential. Thus, the OER contributes to the overall anodic current in the electrolyte containing 2 M NaOH with 1.0 M urea (Figure 2a). Notably, two oxidation peaks with peak current densities appear at ∼0.2 and ∼0.4 V, attributed to the Co^{2+}/Co^{3+} and Ni^{2+}/Ni^{3+} redox couples in an alkaline solution, respectively. This minor redox chemistry is also reflected in X-ray photoelectron spectroscopy (XPS) measurements shown in Figure 5 (to be discussed later), showing a moderate increase of Ni^{3+} and Co^{3+} concentrations on the catalyst surface at low potentials, where UOR is not catalyzed in this potential range.

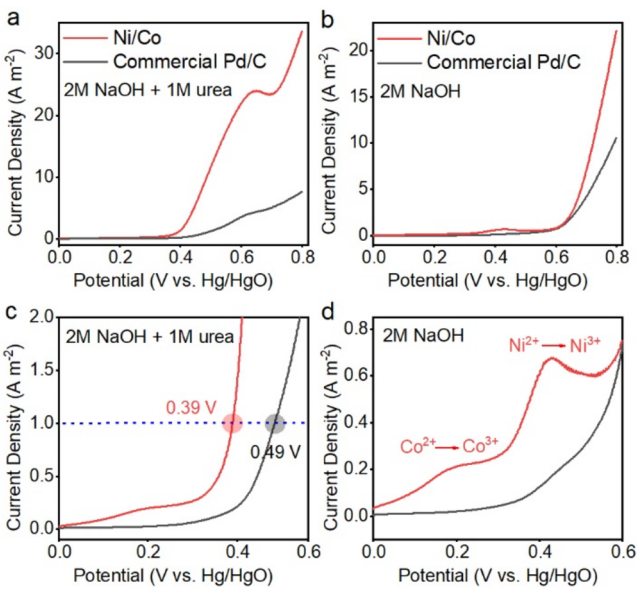

Figure 2. Linear sweep voltammetry of Ni/Co oxide and hydroxide heterostructures and commercial Pd/C in (a, c) 2 M NaOH/1 M urea and (b, d) 2 M NaOH solutions. Zoom-in regions show (c) the potential difference in catalyzing UOR at a current density of 1 A m^{-2} and (d) Co^{2+}/Co^{3+} and Ni^{2+}/Ni^{3+} redox in NaOH solution.

To better distinguish the UOR current from the OER current and eliminate the capacitive current contribution from the high-surface-area carbon support, the staircase voltammetry of UOR (in NaOH/urea) and OER (in NaOH) was performed. Unlike the common linear sweep voltammetry (Figure 2), where the external voltage is swept linearly in time, the voltage is swept in a series of stair steps in the staircase voltammetry, and the current is measured at the end of each potential step (Figure 3a). Notably, the current−time response in each stair step is nearly identical with conventional chronoamperometry measurements, as shown in a schematic drawing in Figure 3b. As with all pulsed electrochemical techniques, when the potential is applied, redox-active species (e.g., urea and water molecules) rapidly adsorbed on the catalyst surface on the working electrode (the peak current at the increased potential is the capacitive current due to urea or water adsorption, shadowed in light blue in Figure 3b), followed by oxidation reactions (redox current due to UOR and OER shaded in pink in Figure 3b). Therefore, the capacitive current increases proportionally with the increasing potential stair steps at the lower voltage when the OER and UOR do not occur, following the electrical double-layer behavior (Figure S5). At the augmented potential, the redox-active species (e.g., urea and water) adsorbed on the catalyst surface are quickly consumed, and the redox current response falls into the diffusion-controlled region, showing exponential decay following the Cottrell equation (Figure 3b).

Figures 3c,d show the current−potential curve, in which the current densities were obtained from staircase voltammetry measurements after 200 s at each voltage stair step. The overall anodic current density (i_A) from the NaOH/urea electrolyte, the OER current density (i_{OER}) from the NaOH electrolyte, and the calculated UOR current density ($i_{UOR} = i_A - i_{OER}$) at each potential stair step are plotted in Figures 3c−e, respectively. The results demonstrate that while i_A increased rapidly with the external potential applied, contributions from i_{OER} and i_{UOR} varied over different voltage ranges. Specifically, the UOR occurred at a lower potential than OER on Ni/Co catalysts. While i_{UOR} is discernible at 0.4 V and increased quickly at 0.5 V, i_{OER} makes only a marginal contribution to the i_A when the potential is less than 0.6 V but becomes dominant when the external potential is beyond 0.6 V.

https://doi.org/10.1021/acs.jpclett.3c03257
J. Phys. Chem. Lett. 2024, 15, 81−89

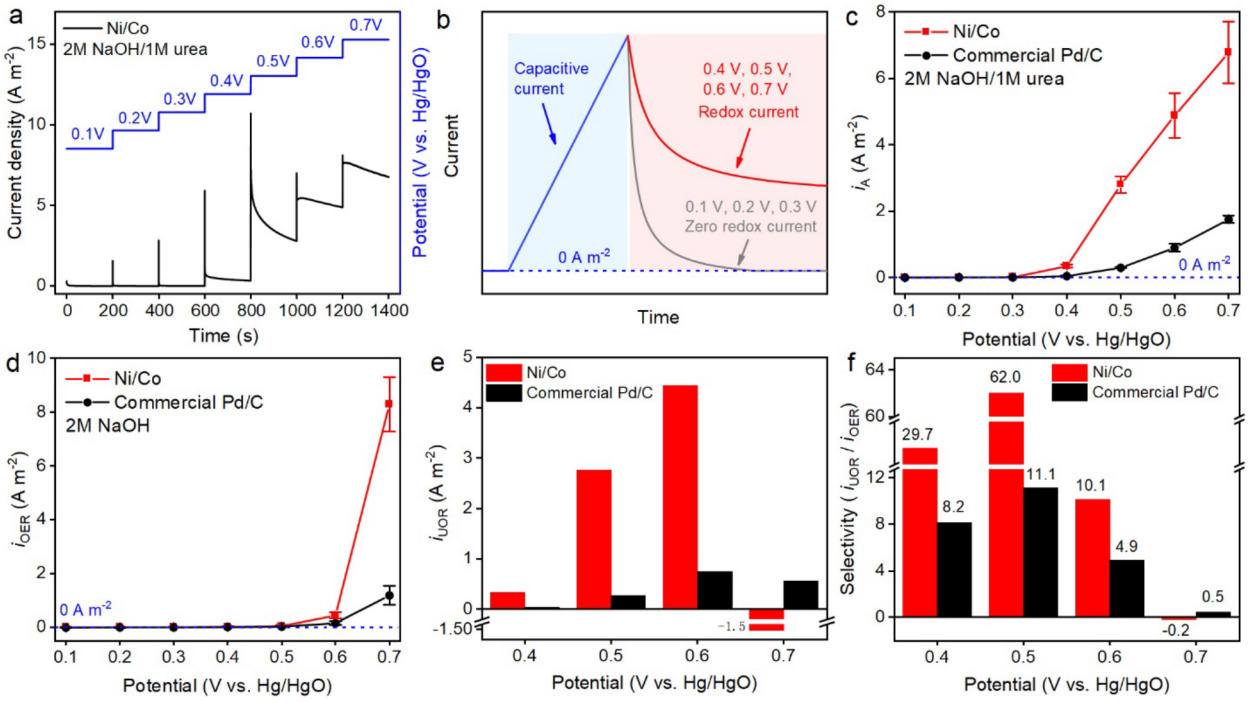

Figure 3. (a) Stairstep voltammetry profiles and (b) schematics of single-step stairstep voltammetry. Summarized stairstep voltammetry data of Ni/Co and commercial Pd/C show (c) anodic current i_A obtained in 2 M NaOH and 1 M urea, (d) the OER current i_{OER} obtained in 2 M NaOH, (e) the UOR current i_{UOR}, and (f) the selectivity of UOR against the OER, all in functions of the potential.

UOR current density is defined in this study as the difference between overall current and the corresponding OER current ($i_{UOR} = i_A - i_{OER}$). It is important to note that this expression is a simple form of estimating the UOR current density and is valid when the reaction kinetics of UOR and OER do not affect each other, especially at the low potential range (e.g., 0–0.6 V). Our electrochemical results suggested that when the potential increases beyond 0.6 V, i_{OER} becomes even higher than i_A. UOR current (i_{UOR}) became a negative value at 0.7 V, which is not a meaningful presentation of anodic current (since a negative current would suggest a cathodic current occurring in the reduction process). This result confirmed a competitive absorption scheme of water and urea molecules on the Ni/Co catalyst surface at high potential (e.g., >0.6 V). In this context, even when the OER is favored at high potential, urea molecules may still occupy some active sites and impede water oxidation kinetics, evidenced by the higher value of i_{OER} than i_A at 0.7 V.

Figure 3f shows the UOR selectivity (S_{UOR}) at various voltages, calculated by eq 5

$$S_{UOR} = \frac{i_{UOR}}{i_{OER}} \tag{5}$$

where Ni/Co catalysts show superior UOR selectivity compared to benchmark Pd/C catalysts within the entire redox-active potential range (0.4–0.7 V), reaching a maximum value of S_{UOR} at 0.5 V. Notably, a negative value of S_{UOR} on Ni/Co catalyst at 0.7 V results from the negative i_{UOR}, as shown in Figure 3e. Nevertheless, the observed potentiodynamic evolutions of i_{OER}, i_{UOR}, and S_{UOR} intuitively demonstrate the feasibility of maintaining plausible UOR kinetics at low voltage (e.g., 0.5 V using Ni/Co catalysts in this study) and altogether avoiding OER. The stability of Ni/Co toward UOR was assessed via long-term (10 h) stairstep voltammetry testing at 0.5 V. The UOR activity of Ni/Co after a 10 h reaction is significantly higher than commercial Pd/C (0.43 A cm^{-2} vs 0.01 A cm^{-2}). Figure S1c shows the crystallographic structures of the Ni/Co oxide samples after the 10 h UOR reaction at 0.5 V compared to Ni/Co samples at the pristine state and after staircase voltammetry at 0.5 V (200 s reaction). The weight ratios of the crystalline phases, including Ni or Co oxides ($M^{II}O$), spinel ($M^{II,III}{}_3O_4$), hydroxides ($M^{II}(OH)_2$), and oxyhydroxide ($M^{III}OOH$), are summarized in Table S2. Notably, the molar ratios of various phases remain similar after the long-term (10 h reaction) UOR compared to the short-term staircase voltammetry measurement (200 s reaction). Ni/Co catalysts show much better stability than the recently reported $Ni_2Fe(CN)_6$ catalyst, which was converted into Ni and Fe oxyhydroxides after 10 h UOR measurements.

It is known that the composition substantially affects the catalytic properties of a multicomponent catalyst. We have also constructed a systematic investigation on a series of Ni/Co oxides with Ni/Co molar ratios of 1:0, 0:1, 2:1, 1:1, and 1:2 to explore the influence of Ni and Co contents on the UOR efficiency. The synthetic details can be found in the Experimental Methods section. Their electrochemical characterizations are summarized in Figures S7 and S8. The optimal composition for catalyzing UOR is a Ni/Co mixed oxide with a Ni/Co molar ratio of 1:1, presented in Figures 1–3. Ni_1/Co_1 decreases the energy barrier to catalyze UOR, requiring a potential of 0.39 V (vs Hg/HgO) to deliver a current density of 1 A m^{-2}, significantly lower than NiO (0.45 V), NiOOH (0.54 V), and Co_3O_4 (0.65 V) but similar to Ni_2/Co_1 (0.39 V) and Ni_1/Co_2 (0.39 V). Notably, the NiO and Co_3O_4 catalysts are far less UOR-active than various Ni/Co catalysts, signifying the synergistic interaction between Ni and Co species on the

https://doi.org/10.1021/acs.jpclett.3c03257
J. Phys. Chem. Lett. 2024, 15, 81–89

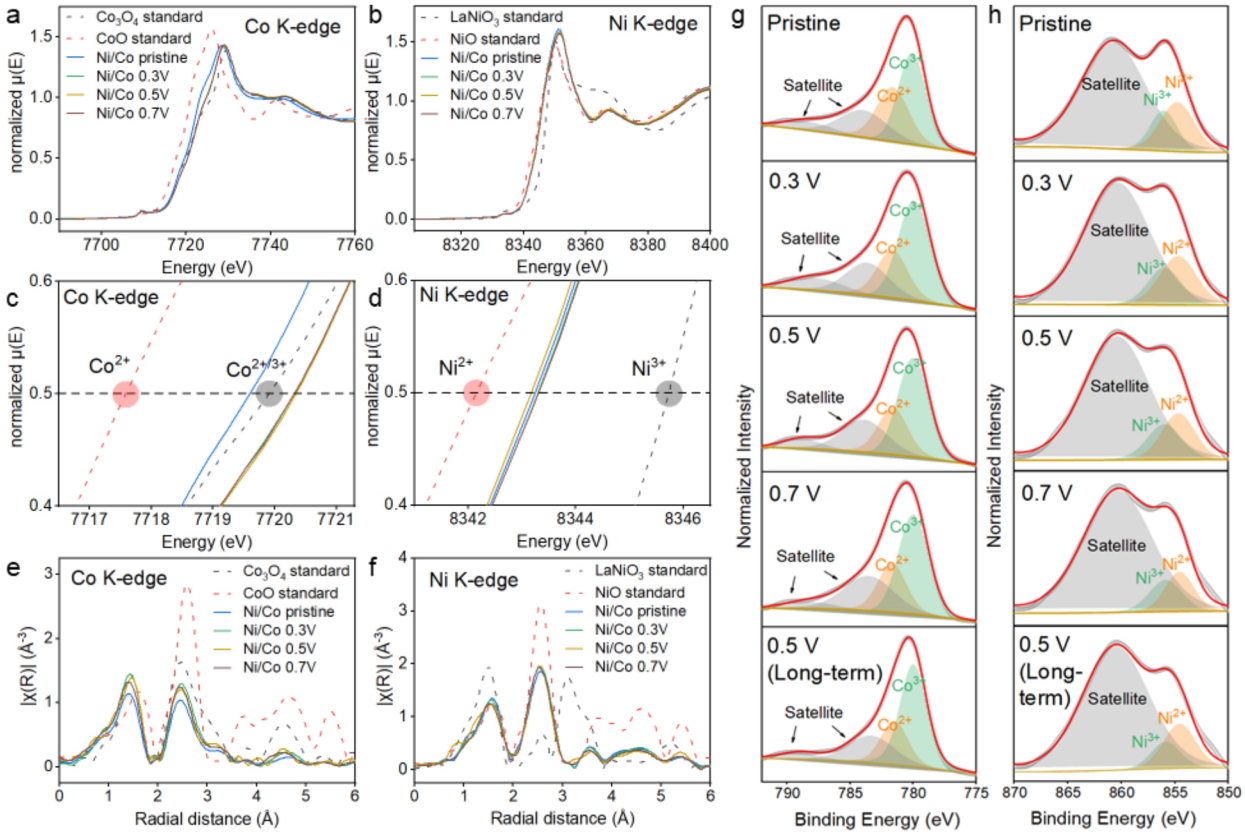

Figure 4. XANES spectra of the Ni/Co catalysts, including K-edge data of (a, c, e) Co and (b, d, f) Ni components in (a, b, c, d) energy space and (e, f) radial space. XPS spectra of Ni/Co catalysts of (g) Co $2p_{3/2}$ and (h) Ni $2p_{3/2}$ at the pristine state and the UOR conditions of 0.3 0.5, and 0.7 V and long-term holding at 0.5 V.

improved catalytic UOR behavior by allowing UOR to take place at lower onset potentials and energy barriers.

Figures 4a,b show Co and Ni K-edge X-ray absorption near-edge structure (XANES) spectra from the Ni/Co catalyst (Ni_1/Co_1) at the pristine state and the potentials of 0.3 V (nonreactive), 0.5 V (UOR-active), and 0.7 V (OER-active), along with Ni and Co standards, including $Ni^{II}O$, $LaNi^{III}O_3$, $Co^{II}O$, and $Co^{III}{}_2Co^{II}O_4$. Notably, the Ni components in Ni/Co after the UOR process at different potentials showed similar valence states compared to those of pristine Ni/Co. A linear fit of absorption energy at the half-edge step [$^1/_2\mu(E)$] between Ni^{2+} and Ni^{3+} from NiO and $LaNiO_3$ standards suggests a Ni valence state of +2.29. On the other hand, the Co components in Ni/Co showed similar valence states at different potentials with a valence around +2.79 through the linear fit of $^1/_2\mu(E)$ energy positions between Co^{2+} and $Co^{2+/3+}$ (1/3 of Co atoms in 2+ and 2/3 in 3+ from Co_3O_4 spinel), higher than that of pristine Ni/Co (+2.55).

To further study the changes in the local structure of the Ni/Co catalyst before and after UOR, the corresponding Fourier transfer EXAFS was plotted in *R*-space (Figures 4e,f) to demonstrate the radial distribution function of the central Ni or Co atom. The strong peaks at ∼1.5 and ∼2.5 Å can be identified as M−O (M: Co or Ni) and M−M backscattering, respectively. There is no discernible shift in the radial distance of both species in *R*-space, indicating that the chemical bonding structure (e.g., M−M and M−O bond length) remained unchanged before and after UOR. However, unlike Ni, the Co *R*-space plot demonstrated a significant increase in Co−Co and Co−O scattering intensity as the potential increased. This feature demonstrates an increasing order of the Co local coordination environment, indicative of structural reconstruction of the Co component to a more stabilized Co−Co and Co−O bonding during the UOR.

The surface valence evolution of the Ni/Co catalyst during UOR was examined by X-ray photoelectron spectroscopy (XPS) to reveal the UOR-active valence of Ni and Co. Figure 4g,h shows the multiplet splitting of Ni and Co $2p_{3/2}$ spectra of the Ni/Co catalysts prepared at different states, including the pristine condition, 0.3 V (nonreactive), 0.5 V (UOR-active), and 0.7 V (OER-active), and the full spectra are shown in Figure S9. In the high-resolution Ni 2p spectrum of the Ni/Co depicted in Figure 4h, the 854.5 and 856.1 eV peaks can be associated with the metallic Ni^{2+} and Ni^{3+} species, respectively. The broad peak centered at ∼861 eV is described as the shake satellite, arising from ionization to excited states of the core ions.[23] Similarly, Co $2p_{3/2}$ of Ni/Co was curve-fitted with a peak at 780.2 eV ascribed to Co^{3+} in octahedral sites, with a peak at 781.8 eV assigned to Co^{2+} in tetrahedral sites.[24] The resulting ratios of Ni^{3+}/Ni^{2+} and Co^{3+}/Co^{2+} are analyzed and are summarized in Table 1.

The Co^{3+}/Co^{2+} ratio increased significantly from 1.34 (pristine) to 2.03 (0.3 V though at which neither UOR nor OER occurs) due to the $Co^{2+} \rightarrow Co^{3+}$ redox in an alkaline solution, also observed in Figure 2d. The Co^{3+}/Co^{2+} ratios remain similar in value (average of 2.0) at 0.3 V (nonreactive), 0.5 V (UOR-active), and 0.7 V (OER-active), suggesting dominant and stable Co^{3+} species on the Ni/Co surface in catalyzing both UOR and OER. Meanwhile, samples at the pristine state and 0.3 V showed similar Ni^{3+}/Ni^{2+} ratios (0.65

https://doi.org/10.1021/acs.jpclett.3c03257
J. Phys. Chem. Lett. 2024, 15, 81−89

Table 1. Ratios of Ni^{3+}/Ni^{2+} and Co^{3+}/Co^{2+} for Ni/Co Catalysts Obtained from XPS

	Ni^{3+}/Ni^{2+}	Co^{3+}/Co^{2+}
pristine	0.65	1.34
0.3 V	0.68	2.03
0.5 V	0.80	2.02
0.7 V	0.91	1.97
0.5 V (long-term)	0.54	2.31

vs 0.68). The Ni^{3+}/Ni^{2+} ratio increased to 0.8 at 0.5 V due to $Ni^{2+} \rightarrow Ni^{3+}$ redox, typically observed in Ni^{2+}-containing oxides and hydroxides in an alkaline solution at ~0.4 V (Figure 2d). When the potential increased to 0.7 V, the Ni^{3+}/Ni^{2+} ratio reached a maximum of 0.91, showing a high anodic current but poor UOR selectivity against the OER (Figure 3f).

Interestingly, Ni/Co catalysts showed a decreased Ni^{3+}/Ni^{2+} ratio (0.80 → 0.54) and an increased Co^{3+}/Co^{2+} ratio (2.02 → 2.31) after long-term UOR (10 h reaction at 0.5 V) compared to short-term UOR measurement (200 s reaction at 0.5 V), though they had nearly identical crystalline structures from XRD measurements (Figure S1). The increased Co^{3+} concentration after long-term reactions agrees with the oxidative *electrochemical* conditions at a positive voltage (0.5 V) where the UOR occurs. On the other hand, the increased Ni^{2+} concentration after long-term reactions could be explained by the *chemical* reduction of Ni^{3+} species during long-term contact with urea molecules. This also further suggests that Ni sites are more actively interacting with urea molecules compared with Co sites (otherwise, chemical reduction of Co^{3+} to Co^{2+} by urea would occur). The long-term XPS results thus highlight the synergistic interaction between Ni and Co sites in catalyzing UOR. It can be inferred that Ni sites actively adsorb and deprotonate urea molecules. At the same time, Co sites dissociated adsorbed water to generate hydroxyl radicals (*OH) to remove reaction intermediates on the catalyst surface to complete the oxidation to N_2, CO_2, and H_2O.

We conducted density functional theory (DFT) calculations to better understand the promotional role of Ni/Co mixed oxide/hydroxide catalysts on the UOR (Figure 5). We simulated NiO (110) and Co_3O_4 (110) model catalysts and also built a NiO/Co_3O_4 mixed oxide interface using a similar method used previously[25] to simulate Ni/Co mixed oxides (where Ni^{2+} and Co^{3+} are dominant components). Figure 5a shows the structures we modeled and results from our calculations. The Bader charges of the above models were calculated, evidencing electron density redistribution with electron transfer from NiO to Co_3O_4. We also calculated the density of states (DOS). The NiO/Co_3O_4 mixed oxide shows distinct DOS features, with a lower work function value (4.72 eV) than NiO (4.95 eV) and Co_3O_4 (5.44 eV). This shift in valence electrons to higher energy levels (closer to a vacuum) is indicative that these valence electrons may be better prepared to participate in bonding between the interfacial surface and adsorbates. Figure 5b also indicates that the lowest unoccupied molecular orbitals (LUMO) at the interface shift to lower energies, approximately 0.4 eV above the Fermi level, much lower than those of NiO (2 eV above the Fermi level) and Co_3O_4 (1.4 eV above the Fermi level). We have ignored the small gap state in Co_3O_4 because it has a very low DOS or occupation. Notably, the bandgap of the NiO/Co_3O_4 interface is much narrower than those of NiO and Co_3O_4, which may be attributed to the electron transfer from NiO to Co_3O_4 at the interface. The reduced bandgap energetically favors the addition of electrons to the bottom of the conduction band by extracting electrons from the top of the valence band. This can lead to easier adsorption of urea and water molecules at the NiO/Co_3O_4 interface and ultimately facilitate urea oxidation processes, observed experimentally (Figures 2 and 3).

In summary, this study showed that homogeneously mixed Ni/Co oxides and hydroxides heterostructures with dominant Ni^{2+} and Co^{3+} species and tailored electronic structure actively catalyze UOR with low onset potential and fast reaction kinetics, superior to NiO, NiOOH, and Co_3O_4 counterparts, as well as commercial Pd/C catalysts. Interestingly, our results suggested that Ni/Co oxides showed high selectivity toward UOR against OER at a low potential range (0.4–0.6 V vs Hg/HgO). At a higher potential range (>0.6 V), oxidation of Ni^{2+} into Ni^{3+} was observed, accompanied by a significant OER current. This work highlights the importance of tuning the valence details for designing high-performance and highly selective UOR electrocatalysts against OER.

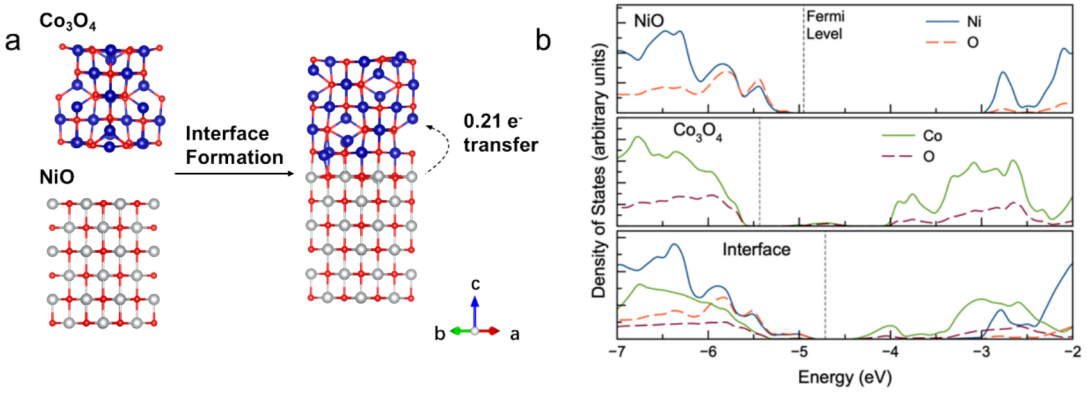

Figure 5. Density functional theory results show (a) the surfaces and interface modeled in this work and (b) the density of states for the three structures. All energies are relative to the vacuum. The Fermi level for each system is also indicated. Formation of the interfaces leads to electron transfer from NiO to Co_3O_4. Formation of the interface also leads to a decrease in the work function (shifting up of valence electron energies) and narrows the bandgap to bring the LUMO energies closer to the Fermi level.

https://doi.org/10.1021/acs.jpclett.3c03257
J. Phys. Chem. Lett. 2024, 15, 81−89

EXPERIMENTAL METHODS

Material Synthesis. The following chemicals were used for the synthesis as purchased: nickel nitrate hexahydrate ($Ni(NO)_3{\cdot}6H_2O$, 99%, Acros Organics), cobalt nitrate hexahydrate ($Co(NO)_3{\cdot}6H_2O$, 99%, Acros Organics), sodium hydroxide (NaOH, 99.99%, ThermoFisher), urea ($CO(NH_2)_2$, 99%, ThermoFisher), Vulcan XC-72 (Fuel Cell Store), palladium (20% Pd on Vulcan XC-72, Premetek), and Nafion 117 (5%, Sigma-Aldrich). All of the chemicals were directly used without further purification.

Synthesis of Ni/Co Catalysts. $Ni(NO)_3{\cdot}6H_2O$ and $Co(NO)_3{\cdot}6H_2O$ with different molar ratios (0.5:0.5, 0.5:1, 1:0.5, 1:0, and 0:1, mmol) were added to a solution containing 75 mL of deionized water, and 5 mmol of urea was then added to the above solution with stirring. The solution was transferred to a Teflon-lined stainless steel autoclave for hydrothermal treatment at 120 °C for 6 h and then cooled to room temperature under ambient conditions. The product was filtrated and washed with deionized water and ethanol, respectively. Afterward, the sample was dried in a vacuum at room temperature for 12 h. Finally, the samples were heated to 400 °C for 3 h in the air to obtain the black powders. The final materials were obtained and named Ni_1/Co_1(Ni:Co 0.5:0.5, mmol), Ni_1/Co_2 (Ni:Co 0.5:1, mmol), Ni_2/Co_1 (Ni:Co 1:0.5, mmol), NiO (Ni:Co = 1:0, mmol), and Co_3O_4 (Ni:Co = 0:1, mmol).

Synthesis of NiOOH. 680 mg of $Ni(NO_3)_2{\cdot}6H_2O$ was dissolved in 100 mL of DI water in a 250 mL flask, and the solution was magnetically stirred at 500 rpm at room temperature in the open air. NaOH with a concentration of 0.124 g mL^{-1} was injected into the stirring solution with a rate of 0.167 mL min^{-1} for 33.5 min using a programmed syringe pump. The light-green precipitate was formed, and then 93 mg of XC72 was added to the flask. The suspension was under stirring overnight to obtain the black powders. After that, the powders were thoroughly washed with deionized water and ethanol and then vacuumed-dried at room temperature for 12 h. Nickel oxyhydroxide was then synthesized by the electrochemical method: 20 μg of the as-made powders was coated on the glassy carbon and then ramped from OCP to 0.6 V in 2 M NaOH by the LSV method with a scan rate of 10 mV/s. Finally, the product was obtained by holding the potential at 0.6 V for 10 min.

Electrochemical Tests. Half-cell measurements were conducted in a CH Instruments 660D/E electrochemical potentiostat using three-electrode half-cells, including glassy carbon drop-coated with active material as the working electrode, platinum wire as the counter, and mercury/mercury oxide as the reference electrode (all from Pine Research Instrumentation). The coating ink was prepared using the 7:3 ratio of active material to XC 72 active carbon mixture in deionized water; 20 μg of active material and 20 μL of 1% Nafion 117 were loaded on the working electrode. The electrolyte consisted of sodium hydroxide and urea, and all electrolytes were degassed using flowing argon gas for at least 30 min before every measurement. Before the electrochemical test, each Ni/Co catalyst (Ni_1/Co_1, Ni_1/Co_2, and Ni_2/Co_1) was preconditioned in 1 M NaOH under the potential window of −1.2 V to 0.6 V with a scan rate of 10 mV/s for 1.5 cycles (starting from OCP to −1.2 V and finally stopping at 0 V after cycles).

Structural Characterizations. X-ray photoelectron spectroscopy (XPS) was performed in a Kratos Axis Supra XPS instrument at the University Instrumentation Center (UIC), University of New Hampshire, using the Al Kα monochromator. The XPS samples were weighed 6 mg with a 7:3 ratio of active material and carbon black loaded on the carbon papers and collected after conducting three-electrode measurements. These electrodes were stopped at different potentials studied in an ultrahigh vacuum of approximately 10^{-8} Torr. CasaXPS software was used to process and analyze the obtained results, and all of the spectra were calibrated according to the adventitious carbon (C 1s) peak at the binding energy of 284.8 eV.

High-resolution transmission electron microscopy (HR-TEM) was conducted at the Electron Microscopy Facility at the Center for Functional Nanomaterials in Brookhaven National Laboratory. The instrument used for the high-angle annular dark-field (HAADF) image was the FEI Talos F200x scanning/transmission electron microscope equipped with an X-FEG electron source module and operated at 200 keV. The elemental mapping of the discharge sample was done by a four-quadrant 0.9 sr energy-dispersive X-ray spectrometer (EDS).

The synchrotron X-ray diffraction (XRD) studies were conducted at beamline 28-ID-1 of Brookhaven National Laboratory. The XRD images were collected on a 2D array detector. All of the acquired patterns were phase analyzed by the Rietveld refinement method in the GSAS-II software. The synchrotron instrument parameters were calibrated by the peak fitting of the CeO_2 standard. The radiation wavelength is 0.1665 Å.

XAS measurements were done at beamline 6-BM Beamline for Materials Measurement at the National Synchrotron Light Source-II, Brookhaven National Laboratory. The XAS measurements were performed in transmission mode at the Ni and Co K-edge. Metal foil and metal oxide powders were used as references for X-ray energy calibration and data alignment. Athena software from the Demeter package was used to perform XAS data processing and analysis.

Density Functional Theory Methodology. We modeled NiO and Co_3O_4 with spin-polarized DFT calculations using the Vienna ab initio Simulation Package (VASP).[26] Valence was treated by a plane-wave basis set with a cutoff energy of 450 eV, while core electrons were treated by projector augmented wave (PAW) potentials.[27] The number of valence electrons is as follows: 10 (Ni), 9 (Co), and 6 (O). We employed the Perdew−Burke−Ernzerhof (PBE) exchange-correlation functional[28] for all calculations and included DFT +U corrections[29] on Fe (4 eV) and Co (4 eV) atoms. Typical values of U used in the literature for Co in Co_3O_4 for instance vary from 3.0 to 6.7 eV.[30−32] Typical values of U used in the literature for Ni in NiO for instance vary from 3.8 to 6.3 eV.[33] Our U values fall within the range of literature values. We also set the initial magnetic moments of these two materials according to ground states identified in the literature.[32,34] We utilized Gaussian smearing with a sigma value of 0.05 eV. We used the VASPKIT program[35] to determine vacuum levels and work functions.

We initially determined the lattice parameters for bulk NiO and Co_3O_4. Our calculated lattice parameters (8.39 Å for NiO and 8.14 Å for Co_3O_4) agree well with literature.[34,36] From these bulk materials we created the (100) surfaces of both Co_3O_4 and NiO. These surfaces have been identified in the literature as very stable due to low surface energies.[30,37] Several

https://doi.org/10.1021/acs.jpclett.3c03257
J. Phys. Chem. Lett. 2024, 15, 81−89

possible terminations exist for the (100) surface of Co_3O_4. Montoya and Haynes[30] identified the most stable surface to terminate in a tetrahedral Co atom, which subsequently relaxes into the surface. We modeled this termination. Shown in Figure 5 are the surface slabs we modeled. Furthermore, these surfaces have similar lattice vector lengths (3% difference), making them amenable to the creation of an interface between the two materials. An interface was created by bringing the two surfaces in contact with each other and allowing both the atomic positions and cell shape to be optimized (VASP setting of ISIF = 4). Allowing the simulation cell to change minimized stresses due to different lattice vector sizes of the two materials at the interface. We simulated several different interfaces with the two surfaces translated by different amounts along the *x* and *y* directions. The lowest energy interface was used in our analysis and shown in Figure 5.

■ ASSOCIATED CONTENT

Supporting Information

The Supporting Information is available free of charge at https://pubs.acs.org/doi/10.1021/acs.jpclett.3c03257.

Supplementary figures on electrochemical measurements (PDF)

■ AUTHOR INFORMATION

Corresponding Author

Xiaowei Teng − *Department of Chemical Engineering, Worcester Polytechnic Institute, Worcester, Massachusetts 01609, United States;* orcid.org/0000-0001-9547-7175; Email: xtemg@wpi.edu

Authors

Tongxin Zhou − *Department of Chemical Engineering, Worcester Polytechnic Institute, Worcester, Massachusetts 01609, United States*

Sathya Narayanan Jagadeesan − *Department of Chemical Engineering, Worcester Polytechnic Institute, Worcester, Massachusetts 01609, United States;* orcid.org/0000-0002-1034-3862

Lihua Zhang − *Center for Functional Nanomaterials, Brookhaven National Laboratory, Upton, New York 11973, United States*

N. Aaron Deskins − *Department of Chemical Engineering, Worcester Polytechnic Institute, Worcester, Massachusetts 01609, United States;* orcid.org/0000-0002-0041-7960

Complete contact information is available at: https://pubs.acs.org/10.1021/acs.jpclett.3c03257

Notes

The authors declare no competing financial interest.

■ ACKNOWLEDGMENTS

This research received financial support from the National Science Foundation under Award No. 2236704 (T.Z., S.N.J., X.T.). This research used the FEI Talos 200X of the Center for Functional Nanomaterials (CFN), which is a US Department of Energy Office of Science User Facility at Brookhaven National Laboratory under Contract No. DE-SC0012704. This research used 28-ID-1 and 6-BM beamlines of the National Synchrotron Light Source II, a US Department of Energy (DOE) Office of Science User Facility operated for the DOE Office of Science by Brookhaven National Laboratory under Contract No. DE-SC0012704. We thank Dr. Bruce Ravel for assisting with the XAS experiments at Beamline 6-BM.

■ REFERENCES

(1) Shih, A. J.; Monteiro, M. C. O.; Dattila, F.; Pavesi, D.; Philips, M.; da Silva, A. H. M.; Vos, R. E.; Ojha, K.; Park, S.; van der Heijden, O.; et al. Water electrolysis. *Nat. Rev. Methods Primers* **2022**, *2* (1), 84. Terlouw, T.; Bauer, C.; McKenna, R.; Mazzotti, M. Large-scale hydrogen production via water electrolysis: a techno-economic and environmental assessment. *Energy Environ. Sci.* **2022**, *15* (9), 3583−3602.

(2) Rollinson, A. N.; Jones, J.; Dupont, V.; Twigg, M. V. Urea as a hydrogen carrier: a perspective on its potential for safe, sustainable and long-term energy supply. *Energy Environ. Sci.* **2011**, *4* (4), 1216−1224.

(3) Boggs, B. K.; King, R. L.; Botte, G. G. Urea electrolysis: direct hydrogen production from urine. *ChemComm* **2009**, *32*, 4859−4861.

(4) Kim, J.; Choi, W. J. K.; Choi, J.; Hoffmann, M. R.; Park, H. Electrolysis of urea and urine for solar hydrogen. *Catal. Today* **2013**, *199*, 2−7.

(5) Sun, X.; Ding, R. Recent progress with electrocatalysts for urea electrolysis in alkaline media for energy-saving hydrogen production. *Catal. Sci. Technol.* **2020**, *10* (6), 1567−1581.

(6) Krase, N. W.; Gaddy, V. Synthesis of urea from ammonia and carbon dioxide. *J. Ind. Eng. Chem.* **1922**, *14* (7), 611−615. Xia, M.; Mao, C.; Gu, A.; Tountas, A. A.; Qiu, C.; Wood, T. E.; Li, Y. F.; Ulmer, U.; Xu, Y.; Viasus, C. J.; et al. Solar urea: towards a sustainable fertilizer industry. *Angew. Chem., Int. Ed.* **2022**, *134* (1), e202110158.

(7) Stokstad, E. Ammonia Pollution From Farming May Exact Hefty Health Costs. *Science* **2014**, *343* (6168), 238−238.

(8) Qadir, M.; Drechsel, P.; Jiménez Cisneros, B.; Kim, Y.; Pramanik, A.; Mehta, P.; Olaniyan, O. Global and regional potential of wastewater as a water, nutrient and energy source. *Nat. Resour. Forum* **2020**, *44* (1), 40−51.

(9) Lan, R.; Tao, S.; Irvine, J. T. S. A direct urea fuel cell - power from fertiliser and waste. *Energy Environ. Sci.* **2010**, *3* (4), 438−441.

(10) Forslund, R. P.; Alexander, C. T.; Abakumov, A. M.; Johnston, K. P.; Stevenson, K. J. Enhanced Electrocatalytic Activities by Substitutional Tuning of Nickel-Based Ruddlesden-Popper Catalysts for the Oxidation of Urea and Small Alcohols. *ACS Catal.* **2019**, *9* (3), 2664−2673.

(11) Geng, S.-K.; Zheng, Y.; Li, S.-Q.; Su, H.; Zhao, X.; Hu, J.; Shu, H.-B.; Jaroniec, M.; Chen, P.; Liu, Q.-H.; et al. Nickel ferrocyanide as a high-performance urea oxidation electrocatalyst. *Nat. Energy* **2021**, *6* (9), 904−912.

(12) Li, R.-Q.; Wan, X.-Y.; Chen, B.-L.; Cao, R.-Y.; Ji, Q.-H.; Deng, J.; Qu, K.-G.; Wang, X.-B.; Zhu, Y.-C. Hierarchical Ni3N/Ni0.2Mo0.8N heterostructure nanorods arrays as efficient electrocatalysts for overall water and urea electrolysis. *Chem. Eng. J.* **2021**, *409*, 128240.

(13) Li, P.; Li, W.; Huang, Y.; Huang, Q.; Li, J.; Zhao, S.; Tian, S. Unconventional Phase Synergies with Doping Engineering Over Ni Electrocatalyst Featuring Regulated Electronic State for Accelerated Urea Oxidation. *ChemSusChem* **2023**, *16* (6), e202201921. Li, P.; Li, W.; Huang, Y.; Huang, Q.; Tian, S. 3D Hierarchical-Architectured Nanoarray Electrode for Boosted and Sustained Urea Electro-Oxidation. *Small* **2023**, *19* (30), 2300725.

(14) Hopsort, G.; Latapie, L.; Groenen Serrano, K.; Loubière, K.; Tzedakis, T. Indirect urea electrooxidation by nickel(III) in alkaline medium: From kinetic and mechanism to reactor modeling. *AIChE J.* **2023**, *69*, e18113. Ye, K.; Zhang, D.; Guo, F.; Cheng, K.; Wang, G.; Cao, D. Highly porous nickel@carbon sponge as a novel type of three-dimensional anode with low cost for high catalytic performance of urea electro-oxidation in alkaline medium. *J. Power Sources* **2015**, *283*, 408−415.

(15) Vedharathinam, V.; Botte, G. G. Direct evidence of the mechanism for the electro-oxidation of urea on Ni(OH)2 catalyst in alkaline medium. *Electrochim. Acta* **2013**, *108*, 660−665. Daramola, D. A.; Singh, D.; Botte, G. G. Dissociation Rates of Urea in the Presence

of NiOOH Catalyst: A DFT Analysis. *J. Phys. Chem. A* **2010**, *114* (43), 11513−11521.
(16) Zhang, L.; Wang, L.; Lin, H.; Liu, Y.; Ye, J.; Wen, Y.; Chen, A.; Wang, L.; Ni, F.; Zhou, Z.; et al. A Lattice-Oxygen-Involved Reaction Pathway to Boost Urea Oxidation. *Angew. Chem., Int. Ed.* **2019**, *58* (47), 16820−16825.
(17) Zhu, B.; Liang, Z.; Zou, R. Designing Advanced Catalysts for Energy Conversion Based on Urea Oxidation Reaction. *Small* **2020**, *16* (7), 1906133.
(18) King, R. L.; Botte, G. G. Investigation of multi-metal catalysts for stable hydrogen production via urea electrolysis. *J. Power Sources* **2011**, *196* (22), 9579−9584.
(19) Wu, F.; Ou, G.; Yang, J.; Li, H.; Gao, Y.; Chen, F.; Wang, Y.; Shi, Y. Bifunctional nickel oxide-based nanosheets for highly efficient overall urea splitting. *ChemComm* **2019**, *55* (46), 6555−6558.
(20) Yu, Z.-Y.; Lang, C.-C.; Gao, M.-R.; Chen, Y.; Fu, Q.-Q.; Duan, Y.; Yu, S.-H. Ni-Mo-O nanorod-derived composite catalysts for efficient alkaline water-to-hydrogen conversion via urea electrolysis. *Energy Environ. Sci.* **2018**, *11* (7), 1890−1897.
(21) Wang, P.; Bai, X.; Jin, H.; Gao, X.; Davey, K.; Zheng, Y.; Jiao, Y.; Qiao, S.-Z. Directed Urea-to-Nitrite Electrooxidation via Tuning Intermediate Adsorption on Co, Ge Co-Doped Ni Sites. *Adv. Funct. Mater.* **2023**, *33* (25), 2300687.
(22) Trasatti, S.; Petrii, O. A. Real surface area measurements in electrochemistry. *Pure Appl. Chem.* **1991**, *63* (5), 711−734. McCrory, C. C. L.; Jung, S.; Peters, J. C.; Jaramillo, T. F. Benchmarking Heterogeneous Electrocatalysts for the Oxygen Evolution Reaction. *J. Am. Chem. Soc.* **2013**, *135* (45), 16977−16987.
(23) Bagus, P. S.; Nelin, C. J.; Brundle, C. R.; Crist, B. V.; Ilton, E. S.; Lahiri, N.; Rosso, K. M. Main and Satellite Features in the Ni 2p XPS of NiO. *Inorg. Chem.* **2022**, *61* (45), 18077−18094. Carley, A. F.; Jackson, S. D.; O'Shea, J. N.; Roberts, M. W. The formation and characterisation of Ni3+ — an X-ray photoelectron spectroscopic investigation of potassium-doped Ni(110)-O. *Surf. Sci.* **1999**, *440* (3), L868−L874.
(24) Babar, P.; Patil, K.; Mahmood, J.; Kim, S.-j.; Kim, J. H.; Yavuz, C. T. Low-overpotential overall water splitting by a cooperative interface of cobalt-iron hydroxide and iron oxyhydroxide. *Cell Rep. Phys. Sci.* **2022**, *3* (2), 100762.
(25) Deskins, N. A.; Kerisit, S.; Rosso, K. M.; Dupuis, M. Molecular Dynamics Characterization of Rutile-Anatase Interfaces. *J. Phys. Chem. C* **2007**, *111* (26), 9290−9298.
(26) Kresse, G.; Hafner, J. Ab Initio Molecular-Dynamics for Liquid-Metals. *Phys. Rev. B* **1993**, *47* (1), 558−561. Kresse, G.; Hafner, J. Ab-Initio Molecular-Dynamics Simulation of the Liquid-Metal Amorphous-Semiconductor Transition in Germanium. *Phys. Rev. B* **1994**, *49* (20), 14251−14269. Kresse, G.; Furthmuller, J. Efficient iterative schemes for ab initio total-energy calculations using a plane-wave basis set. *Phys. Rev. B* **1996**, *54* (16), 11169−11186. Kresse, G.; Furthmuller, J. Efficiency of ab-initio total energy calculations for metals and semiconductors using a plane-wave basis set. *Comput. Mater. Sci.* **1996**, *6* (1), 15−50.
(27) Kresse, G.; Joubert, D. From ultrasoft pseudopotentials to the projector augmented-wave method. *Phys. Rev. B* **1999**, *59* (3), 1758−1775. Blöchl, P. E. Projector augmented-wave method. *Phys. Rev. B* **1994**, *50* (24), 17953−17979.
(28) Perdew, J. P.; Burke, K.; Ernzerhof, M. Generalized gradient approximation made simple. *Phys. Rev. Lett.* **1996**, *77* (18), 3865−3868.
(29) Dudarev, S. L.; Botton, G. A.; Savrasov, S. Y.; Humphreys, C. J.; Sutton, A. P. Electron-energy-loss spectra and the structural stability of nickel oxide: An LSDA+U study. *Phys. Rev. B* **1998**, *57* (3), 1505−1509.
(30) Montoya, A.; Haynes, B. S. Periodic density functional study of Co3O4 surfaces. *Chem. Phys. Lett.* **2011**, *502* (1), 63−68.
(31) Peng, Y.; Hajiyani, H.; Pentcheva, R. Influence of Fe and Ni Doping on the OER Performance at the Co3O4(001) Surface: Insights from DFT+U Calculations. *ACS Catal.* **2021**, *11* (9), 5601−5613. Zhang, P.; Dong, Y.; Kou, Y.; Yang, Z.; Li, Y.; Sun, X. First-Principles Study of Oxygen Evolution Reaction on the Oxygen-Containing Species Covered CoII-Exposing Co3O4 (100) Surface. *Catal. Lett.* **2015**, *145* (5), 1169−1176. Zasada, F.; Piskorz, W.; Sojka, Z. Cobalt Spinel at Various Redox Conditions: DFT+U Investigations into the Structure and Surface Thermodynamics of the (100) Facet. *J. Phys. Chem. C* **2015**, *119* (33), 19180−19191.
(32) Singh, V.; Kosa, M.; Majhi, K.; Major, D. T. Putting DFT to the Test: A First-Principles Study of Electronic, Magnetic, and Optical Properties of Co3O4. *J. Chem. Theory Comput.* **2015**, *11* (1), 64−72.
(33) Ferrari, A. M.; Pisani, C.; Cinquini, F.; Giordano, L.; Pacchioni, G. Cationic and anionic vacancies on the NiO(100) surface: DFT+U and hybrid functional density functional theory calculations. *J. Chem. Phys.* **2007**, *127* (17), 174711.
(34) DelloStritto, M. J.; Kaplan, A. D.; Perdew, J. P.; Klein, M. L. Predicting the properties of NiO with density functional theory: Impact of exchange and correlation approximations and validation of the r2SCAN functional. *APL Materials* **2023**, *11* (6), 060702.
(35) Wang, V.; Xu, N.; Liu, J.-C.; Tang, G.; Geng, W.-T. VASPKIT: A user-friendly interface facilitating high-throughput computing and analysis using VASP code. *Comput. Phys. Commun.* **2021**, *267*, 108033.
(36) Saal, J. E.; Wang, Y.; Shang, S.; Liu, Z.-K. Thermodynamic Properties of Co3O4 and Sr6Co5O15 from First-Principles. *Inorg. Chem.* **2010**, *49* (22), 10291−10298.
(37) Xiang, J.; Xiang, B.; Cui, X. NiO nanoparticle surface energy studies using first principles calculations. *New J. Chem.* **2018**, *42* (13), 10791−10797.

https://doi.org/10.1021/acs.jpclett.3c03257
J. Phys. Chem. Lett. 2024, 15, 81−89